Heliyon 11 (2025) e41178

Contents lists available at ScienceDirect

Heliyon

journal homepage: www.cell.com/heliyon

Research article

Molecular dynamics model of mechanophore sensors for biological force measurement

Sumit Mittal [a,**], Rongsheng E. Wang [b], Robert Ros [c,d,e], Alison E. Ondrus [f,***], Abhishek Singharoy [g,*]

[a] School of Advanced Sciences and Languages, VIT Bhopal University, Kothrikalan, Sehore, Madhya Pradesh, 466114, India
[b] Department of Chemistry, Temple University, 1901 N. 13th Street, Philadelphia, PA, 19122, USA
[c] Department of Physics, Arizona State University, Tempe, AZ, 85287, USA
[d] Center for Single Molecule Biophysics, The Biodesign Institute, Arizona State University, Tempe, AZ, 85287, USA
[e] Center for Biological Physics, Arizona State University, Tempe, AZ, 85287, USA
[f] Department of Chemistry and Pharmaceutical Sciences, University of Illinois Chicago, 900 W Taylor St, Science & Engineering Laboratories West South Building #608 Room 2230, Chicago, IL, 60607, USA
[g] School of Molecular Sciences, Arizona State University, Tempe, AZ, 85287, USA

ARTICLE INFO

Keywords:
Mechanophore
QM/MM simulations
Biosensors
Polymer mechanochemistry
DFT

ABSTRACT

Cellular forces regulate an untold spectrum of living processes, such as cell migration, gene expression, and ion conduction. However, a quantitative description of mechanical control remains elusive due to the lack of general, live-cell tools to measure discrete forces between biomolecules. Here we introduce a computational pipeline for force measurement that leverages well-defined, tunable release of a mechanically activated small molecule fluorophore. These sensors are characterized using a multiscale approach combining equilibrium and steered QM/MM molecular dynamics models to capture the chemical, mechanical, and conformational transitions underlying force activation thresholds on a nano Newton scale. We find that chemical modification of the mechanophore and variation of its biomolecular tethers can tune the rate-determining step for fluorophore release and adjust the mechanochemical activation barrier. The models offer a new molecular framework for calibrated, programmable biomolecular force reporting within the live-cell regime, opening new opportunities to study mechanical phenomena in biological systems.

1. Introduction

Mechanical forces generated by cells not only drive bending, stretching, alignment, and repositioning during homeostasis and development but also regulate cellular functions ranging from receptor signaling to differentiation and proliferation [1,2]. Notable recent examples include control of gene expression by mechanical coupling between the cytoskeleton and the nucleus [3], immune cell activation by tension associated with antigen-T cell receptor binding [4], and force-promoted polypeptide elongation by nascent

* Corresponding author.
** Corresponding author. School of Advanced Sciences and Languages, VIT Bhopal University, Kothrikalan, Sehore, Madhya Pradesh, 466114, India.
*** Corresponding author.
E-mail address: asinghar@asu.edu (A. Singharoy).

https://doi.org/10.1016/j.heliyon.2024.e41178
Received 8 June 2024; Received in revised form 12 November 2024; Accepted 11 December 2024
Available online 12 December 2024

protein folding [5]. The measurement of such cellular and sub-cellular forces has been accelerated by seminal advances in force microscopy and optical tweezers [6,7]. Because these techniques can only be applied *in vitro*, tools such as DNA tension probes [8–12], fluorescent protein-based FRET pairs, and a variety of DNA-protein hybrids have been developed to characterize discrete live cell forces. Despite these advances, our understanding of force-accelerated cellular processes is limited by the fact that each technique addresses only a subset of cellular entities, and no general platform is available to evaluate mechanical forces between intracellular biomolecules of interest [13,14]. In this sense, chemical genetic probes based on force-responsive small molecules are ideally positioned to provide facile control of timing, tunability, and multiplexing in a live-cell context. General, calibrated optical probes for direct imaging of cellular forces would enable fundamentally new insights into cell signaling events and mechanisms of pathway regulation [2,8].

We introduce mechanophores as a chemically tunable platform for sub-nano Newton force measurements. Mechanophores are chemical entities that undergo selective, local chemical changes in response to the mechanical strain [15–17] and serve as fundamental tools to optically map real time forces in polymer applications [18]. These molecules have also been coupled with a wide range of mechanical processes, such as force-induced catalysis [19], modulation of electrical conductivity [20], and drug delivery [21]. Fluorescent reporter mechanophores generate an optical signal by linking polymers to a mechanically caged fluorophore that undergoes an uncaging reaction in response to tensile stress [22]. Depending on the applied external stimuli, mechanophores can report local forces anywhere in the vicinity of 100–2000 pN. These features enable direct monitoring of mechanical processes propagated over distances at an intracellular scale. Critically, the chemical unit of the mechanophore is amenable to biorthogonal functionalization, providing opportunities to tether it to diverse biomolecules of interest for cellular force sensing in future experiments. For example, we illustrate in Scheme 1A, to generate tensile forces inside the cell, one end of the mechanophore can be ligated via a HaloTag fusion to a protein of interest while the other end is tethered via a biotin-streptavidin interaction to an immobile surface (e.g., the extracellular matrix).

In this work we describe a modeling framework for force measurements using mechanophore-based fluorescent sensors. Specifically, we explore a computational workflow for evaluating mechanoresponsive processes under non-equilibrium conditions using a combination of multiscale equilibrium and steered molecular dynamics simulations. An implicit assumption in our approach is that in the presence of mechanical stimuli, the chemical event is local and conformational changes are global. Our platform capitalizes on modeling bioorthogonal ligation of small molecule mechanophores to polypeptide linkers that can be genetically incorporated into proteins of interest. We use an exemplary mechanophore consisting of a furan-maleimide cycloadduct that undergoes a force-induced retro-Diels Alder (retro-DA) reaction to yield an unstable 2-furyl carbonate, which decarboxylates to uncage a resorufin fluorophore (Scheme 1B) [23].

First, we use Quantum Mechanical and Molecular Mechanics (QM/MM) calculations to describe a mechanism for the retro-DA reaction and release of the resorufin fluorophore (Fig. 1). We apply this mechanism to a comparative study of reaction energetics

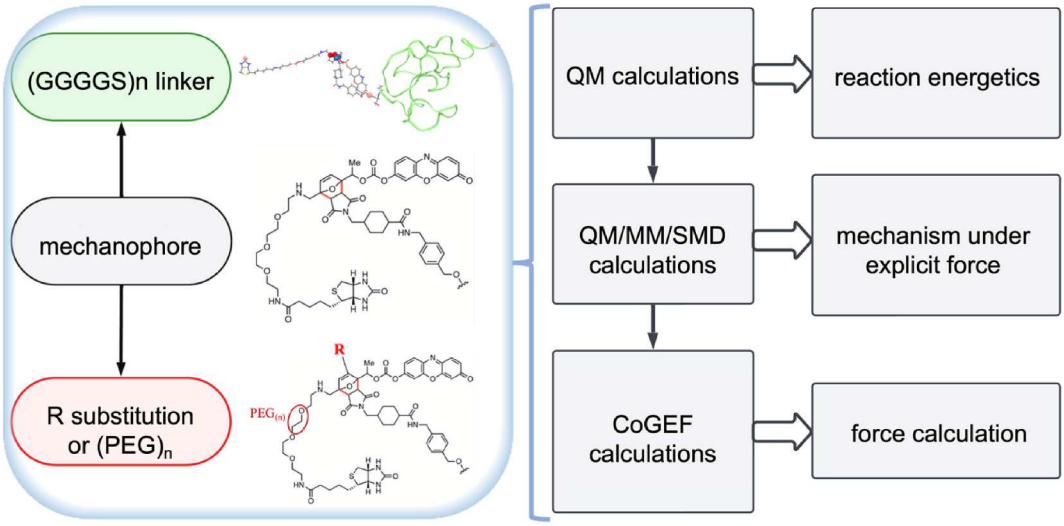

Fig. 1. Computational workflow to investigate mechanical force-induced fluorophore release. A three-step multiscale model is presented. First, the reaction mechanism (i.e., stepwise or concerted) and associated energetics for the retro-Diels Alder reaction are determined by performing potential energy scans at the B3LYP/6-31G//PM3 level of theory. Also, for model systems, forces computed by PM3 are benchmarked against DFT computations by matching the energies (Fig. S10). Second, CoGEF calculations are performed at the PM3 level of theory to compute the mechanophore geometry and bond-rupturing force. Third, the reaction mechanism, energetics, and bond-rupturing force under the influence of explicit external force are obtained by QM/MM/SMD simulations. Here, a terminal atom of the molecule is kept fixed while the other end is pulled with a constant velocity. Next, modified mechanophores containing substitutions at the furan ring or and/or extended PEG linkers are studied by QM and CoGEF calculations to assess relative changes in reaction energies and forces. Finally, the mechanophore molecule coupled to a poly(GGGGS) linker is studied by CoGEF and QM/MM/SMD, where simulations are performed with varying pulling velocities to assess and control relative bond-rupturing forces.

across alternatively substituted mechanophores. Within these examples, we optimize the molecular design for force-sensing by varying the length of the linker moieties that connect the mechanophore to the termini. Our computations elucidate how alternative force environments can be probed using mechanophores of varying lengths and activation energies. *Second*, we integrate the Constrained Geometries simulate External Force (CoGEF) method with QM/MM-Steered Molecular Dynamics (QM/MM-SMD) simulations to obtain reliable force estimates and qualitative trends in energy barriers for models of the full mechanophore system in a realistic solvent environment. This enables us to determine the critical force required to activate the mechanophore and assess how electron donating *vs.* accepting substituents shift this limit. *Finally*, we use the steering simulations to identify a range of velocities, temperatures, and linker lengths over which the mechanical forces are small enough to induce fluorophore release on a timescale compatible with atomic force measurement (AFM) imaging. By accounting for these physical factors, we avoid force overestimates that are encountered by traditional CoGEF computations. Specifically, we use QM/MM-SMD calculations to obtain a unified model of energy, force, and dynamics for a mechanophore-linker system that is designed to enable AFM calibration.

The results from our multi-scale workflow pinpoint the reaction energy barriers, rate-determining step, and critical force needed for mechanophore activation. Our findings match a concerted retro-DA mechanism established previously for model systems, including the energetics of bond breaking for mechanophores bearing electron donating and electron withdrawing substituents. Using this manifold, we introduce chemical modifications to customize the force sensing properties of the probe. It provides a scheme to design and calibrate mechanophores as quantitative, optical reporters of live cell forces for designing new experiments.

2. Results and discussion

2.1. The core mechanophore undergoes concerted retro-Diels Alder and rate-determining fluorophore release

To estimate the forces involved in generating a fluorescent signal from the mechanophore, we first sought to evaluate the two stages of the process, namely: (1) force-induced release of the furan-maleimide adduct and (2) fragmentation and decarboxylation of the resulting 2-furyl carbonate to uncage the resorufin fluorophore (Scheme 1B). We considered that the retro-DA reaction in the first stage could proceed through either a concerted or a stepwise carbon-carbon bond-breaking mechanism [24]. The energetics of these two possible pathways are presented in Fig. 2. As outlined in the Methods section (**M.1**), we first equilibrated geometries of the complete mechanophore molecule using MM force fields and conventional MD simulations. A two-dimensional potential energy surface (2D-PES) was then constructed at a semi-empirical PM3 level of theory by simultaneously considering C1–C6 and C4–C5 bond distances along the reaction coordinate (Fig. S1) [25]. The stationary points on this 2D-PES were optimized at the B3LYP/6-31G level of theory, which we denote collectively as B3LYP/6-31G//PM3 (see Methods **M.1**).

Release of the furan-maleimide adduct. As illustrated in Fig. 2, the concerted pathway features a transition state, denoted TS_C, at 34.93 kcal/mol above the reactant. We further evaluated this TS_C using imaginary vibrational frequency calculations at a B3LYP/6-31G level of theory, which showed that both C1-C6 and C4-C5 elongate from 1.49 Å and 1.56 Å in the reactant to 2.09 Å and 2.16 Å in TS_C, respectively. Comparing the frontier molecular orbitals (FMOs), the highest occupied molecular orbital (HOMO) of the reactant features significant overlap of sigma orbitals (σ) along the C1-C6 and C4-C5 bonds (Fig. S2), whereas these bonds weaken in TS_C and eventually vanish. Concurrently, the lowest occupied molecular orbital (LUMO) of TS_C shows an increasing overlap of π orbitals, indicating the formation of a π bond between C5 and C6 in the maleimide.

For comparison, we also modeled a stepwise pathway (Fig. 2). The first transition state (TS_1) is located at 49.74 kcal/mol above the reactant (RS). This TS_1 features an extended C1-C6 bond length of 2.26 Å, whereas the C4-C5 distance remains similar to the ground state. Following the intrinsic reaction coordinate procedure described above, we also identified an intermediate state (IS) at 19.43 kcal/mol above the reactant. Examination of the IS structure reveals that breaking of the C1-C6 bond enables the furan ring to undergo a large conformational change and adopt a planar geometry, reducing unfavorable steric interactions present in TS_1. A potential energy

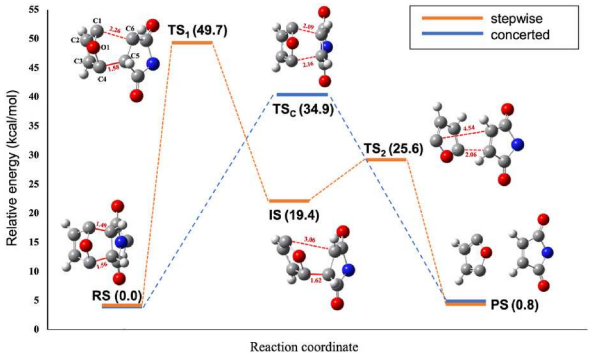

Fig. 2. Concerted and stepwise reaction mechanisms for retro-DA reaction of the mechanophore. Characterization of the retro-DA reaction in water through either a concerted (blue) or a stepwise (orange) pathway at the B3LYP/6-31G//PM3 level of theory using the PCM solvent model. The bond distance between atoms C4 and C5 is used as the reaction coordinate for PES calculations. Conformations of reactant (RS), transition states (TS_C, TS_1, and TS_2), intermediate state (IS), and product (PS) along the reaction coordinate are shown.

scan of the dihedral angles in the furan ring shows that this in-plane movement stabilizes the system by ~21 kcal/mol (Fig. S3). Subsequently, both C4-C5 and C1-C6 bonds elongate toward the next transition state, TS_2, which lies at 25.61 kcal/mol above the reactant. The C1-C6 bond lengthens to 4.54 Å, while the C4-C5 bond stretches slightly to 2.06 Å. Elongation of the C-C bonds is accompanied by rotation of the furan and maleimide rings along the C4-C5 bond axis (Fig. S3). FMO analysis of the TS_2 and IS conformations indicates that the HOMO of IS is dominated by a σ orbital localized on the C1-C6 bond (Fig. S2). Due to changes in the torsion angle about the C4-C5 bond, this σ orbital contribution is missing in TS_2. Consequently, the higher energy of TS_2 relative to IS can be attributed to the loss of the C1-C6 bond. As with the concerted mechanism, the products of the stepwise mechanism are a furan and a maleimide.

Because the activation energy barrier to reach TS_C in the concerted reaction is 14.81 kcal/mol lower (approximately 10 k_BT) than TS_1 of the stepwise mechanism, the concerted mechanism will likely predominate due to kinetics. Importantly, the 34.93 kcal/mol activation barrier for the concerted reaction remains almost 50-fold higher than thermal energy at room temperature, indicating that external perturbations (e.g., an applied force) are required to catalyse the process. A concerted mechanism is also in line with existing computational analyses of the retro-DA reaction of 5,6-dihydro-4-hydroxy-6-methylpyran-2-one using DFT calculations [26], 4-methylcyclohexene using MPW2PLYP calculations [27], and the cycloadduct of cyclopentadiene with 1,4-naphthoquinone using QM/MM (AM1/TIP4P) calculations [28].

Fragmentation and decarboxylation. We next modeled the reaction cascade that produces the fluorescent signal, namely fragmentation of the C12-O4 bond to the 2-furyl carbonate and decarboxylation to release the C14-O6 bond and liberate resorufin (**Scheme 1**). To compute the PES of this sequence, we again employed the B3LYP/6-31G//PM3 (see Methods **M.1**). As illustrated in Fig. S4, the first bond breaking event involves an increase in the bond distance between C12 of the furan substituent and O4 of the CO_2 moiety from 1.50 Å in the initial structure **I** (Fig. S4A) to 2.90 Å at the transition state to form the intermediate products **II**. Subsequently, the C14-O6 bond in **III** (Fig. S4B) increases from 1.48 Å to 2.88 Å in the product **IV**, in which CO_2 is completely detached from resorufin. The final product **V** is energetically more stable than reactant **III** by 17.82 kcal/mol, which correlates with linearization of the CO_2 moiety as the O-C-O angle changes from 128.1° in the starting structure to 178.9° in the product state. The activation energy for C12-O4 fragmentation of the furan substituent is 38.19 kcal/mol, resulting in a barrierless loss of the C14-O6 bond to release CO_2 from resorufin. Significantly, these calculations suggest that both the retro-DA and resorufin decarboxylation are fast relative to expulsion of the furyl carbonate substituent, which has also been implied by kinetic measurements of mechanophore activation [29].

2.2. *Furan substitution and linker length fine-tune mechanophore properties and rate-determining step*

Recent experimental studies have revealed that the 3-position of the furan can be substituted with an electron-donating group to modulate the retro-DA kinetics of the corresponding maleimide-furan adducts [30]. Inspired by this observation, we computed the activation energy barriers of the retro-DA (concerted pathway) and the furyl carbonate fragmentation reactions for a mechanophore bearing a methyl or a phenoxy substituent at the 3-position of the furan unit (Fig. S5). For these calculations, we incorporated a biotin tether via a polyethylene glycol (PEG_3) linker to the furan C1 position. We performed the calculations using the B3LYP/6-31G//PM3 level of theory combined with the polarizable continuum model (PCM) solvent model. Our results show that the phenoxy group reduces the barrier of the retro-DA reaction by ~6 kcal/mol and the fragmentation reaction by ~9 kcal/mol (Fig. S5), which is consistent with experimental rate measurements and theoretical calculations [30]. Interestingly, the two activation energy values, 28.9 kcal/mol and 29.1 kcal/mol, respectively, are comparable in the case of the phenoxy substituted mechanophore, indicating that furan substitution may switch the rate-determining step from the furyl carbonate fragmentation to the retro-DA reaction.

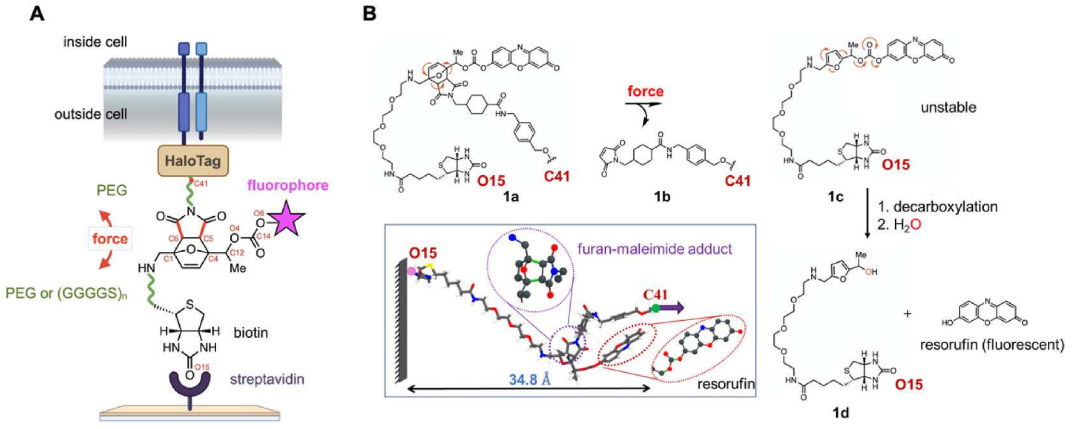

Scheme 1. Mechanical force-induced fluorophore release. **A.** Overall schematic for a genetically incorporated small molecule mechanophore; one end of the mechanophore is attached via a HALO-Tag to a protein of interest; the other end is tethered via a PEG_n or $(GGGGS)_n$ linker to a surface interaction between biotin and streptavidin. **B.** Structure of the mechanophore molecule **1a**. The furan-maleimide adduct (purple circle) is mechanochemically coupled to a caged resorufin fluorophore (red circle). Force-induced retro-Diels Alder reaction of **1a** yields maleimide **1b** and carbonate **1c**, which spontaneously fragments to release fluorescent resorufin and furan **1d**.

We next investigated the possibility of altering the length of the PEG unit to modulate the force required for the mechanochemical reaction [31,32]. Specifically, we varied the length of the PEG linker from 1 to 6 repeats and computed the activation energy value of the retro-DA reaction using the procedure described above. The resulting activation energy increased with PEG length (Fig. S6), varying over a range of 31.7 kcal/mol for PEG_1 to 37.6 kcal/mol for PEG_6 (Table S2). Notably, the activation energy for PEG_6 is comparable to the activation barrier for the C12-O4 bond fragmentation (38.2 kcal/mol). Past higher-level computations of this decarboxylation step have determined this value from anywhere between 23 and 34 kcal/mol [23,29]. So, the computations suggest that lengthening the PEG domain can also modulate the rate-determining step.

Our calculations for increasing PEG linker lengths suggest that the increase in activation energy is associated with reorganization of the linker conformation before the mechanophore undergoes the retro-DA reaction. While significant conformational rearrangement occurs between the starting molecule and the transition state for each full molecule (RMSDs of 3.5–4.0 Å), a comparison of the C1-C6 and C4-C5 bonds and dihedral angles in the furan-maleimide unit shows that the reaction center is similar in all cases (RMSDs of ~0.09 Å) (Table S3). The primary structural change underlying the increasing activation with PEG length is the end-to-end extension of the molecule. Consequently, calculations from pre-stretched PEG conformations show comparable activation energies for PEG_1, PEG_3, and PEG_6 (Table S4).

To determine the combined influence of the furan substituent and PEG linger lengths on the rate of fluorophore release, we used Multiwell software to calculate the canonical rate constants for the retro-DA reaction and the fragmentation reactions based on stationary point geometries (Table S2). We find that the rate of the retro-DA reaction for an unsubstituted mechanophore with six PEG units is higher than fragmentation, and that this trend is reinforced by a furan phenoxy substituent. Altogether, these calculations indicate that the rate-determining step can be tuned by a combination of furan substitution and PEG linker length.

2.3. *Linker extension is a key contributor to mechanophore activation*

Next, we sought a computational method that would allow us to explicitly control the non-equilibrium perturbation (e.g., force) and observe conformational rearrangements of the full mechanophore system within a realistic solvent environment. Multiple methods have been employed to investigate reactivity of mechanoresponsive molecules. Among these, Car-Parrinello Molecular Dynamics (CPMD) simulations [33–37] have been used to study minimal models of mechanophores by performing multiple simulations with end-to-end distances of the molecule constrained to a range of values, then carrying out *a posteriori* force analysis to determine the bond breaking force [38,39]. A practical limitation of CPMD and other *ab initio* MD methods is their computational cost, which limits most studies to small-to-medium sized systems [40]. Typically, this translates to <100 atoms and timescales of tens of picoseconds, which is inadequate for the mechanophore systems of interest. Although classical MD simulations have been used to model the effect of force on unfolding and stretching of large biomolecular systems [41,42], they offer little help for investigating mechanochemistry, as bond-breaking and formation are not captured in molecular mechanics.

Therefore, to measure the reaction energetics and bond rupturing force of the mechanophore in the presence of applied force, we made use of combined Quantum Mechanical and Molecular Mechanics (QM/MM) and explicit solvent all-atom Steered Molecular Dynamics (SMD) simulations to study the reaction pathways that mechanophore takes when activated by external bias. Specifically, we investigated the conformational changes that the mechanophore unit undergoes when being pulled at a constant velocity of 0.06 Å/

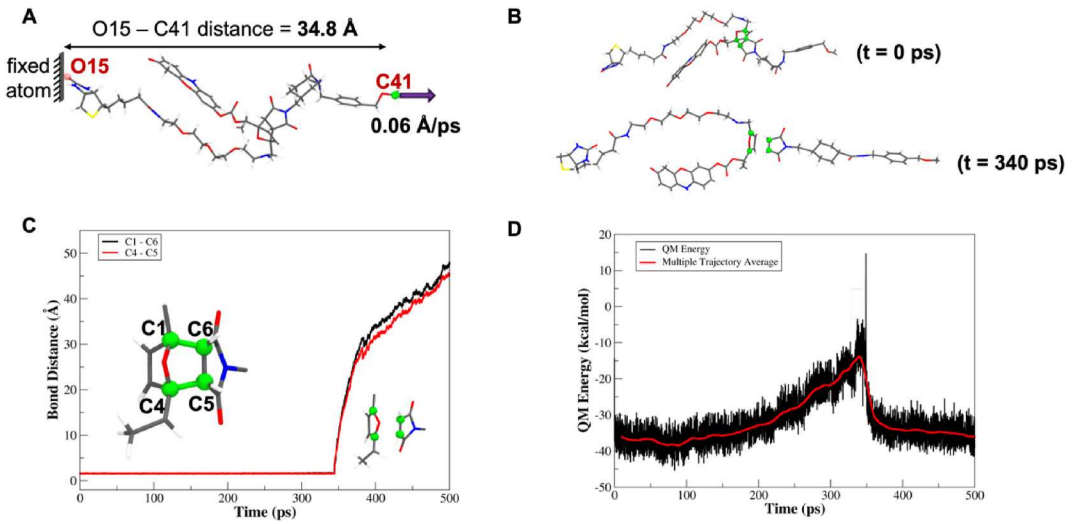

Fig. 3. Retro-DA reaction under external force. **A.** Equilibrated geometry of the mechanophore used for QM/MM/SMD simulation. The terminal atom O15 (pink sphere) is kept fixed while C41 (green sphere) is pulled at a constant velocity. **B.** Conformation of the mechanophore before and after retro-DA reaction during the QM/MM/SMD simulation. **C.** Bond distance over time showing C1-C6 and C4-C5 rupture. **D.** QM energy over time during the QM/MM SMD simulation.

ps over 500 ps (See Methods **M.2**). To accommodate the enhanced system size of the water-solvated mechanophore, we performed simulations on NAMD 2.14, complemented by semi-empirical QM/MM. The QM region (157 atoms), which comprised an unsubstituted mechanophore unit and a PEG_3 linker, was described at the PM3 level of theory. The MM region (83487 atoms), which consisted of the aqueous environment, was described using the CHARMM36m force field. We chose the PM3 method for the preliminary trajectory based on its successful integration with classical MD and SMD simulations [43–45] and past applications for studying DA reactions [46,47]. Because the cost for the low-level sampling at the PM3 level of theory is significantly less than that of single-point energy evaluations at higher levels of theory, these PM3/CHARMM36m SMD simulations provided an enhancement in efficiency of approximately two orders of magnitude over brute-force DFT-based QM/MM models.

As shown in Fig. 3, while the distance between C4-C5 fluctuates around 1.58 ± 0.04 Å for the first 344 ps of the trajectory, it increases to 3.36 Å as the bond is ruptured. A similar change is observed for the C1-C6 bond, which increases to 3.55 Å after varying around 1.59 ± 0.04 Å for the first 344 ps. Interestingly, both bonds rupture simultaneously, further validating a concerted retro-DA mechanism. During the bond-breaking process, the QM energy increases by 23.63 ± 2.18 kcal/mol. The force on the terminal atom being pulled, namely C41, increases gradually as the distance between the terminal atoms, O15 and C41, lengthens from 34.82 to 54.35 Å (Fig. S7). Beyond this end-to-end distance, a sharp increase in the force to 3.34 nN leads to the simultaneous rupture of C1-C6 and C4-C5 bonds, indicating a retro-DA reaction. Significantly, we recovered a concerted reaction mechanism from all three repeats of our QM/MM SMD simulations, which is consistent with the results of our deterministic QM computations in Fig. 2.

Despite the finite timescale of the pulling simulations, in the presence of an external force the reaction barrier fell to 23.63 ± 2.18 kcal/mol, which is significantly less than the 34.93 kcal/mol barrier derived from DFT. This value for the retro-DA reaction of a furan-maleimide mechanophore aligns with the activation energy values of 20–25 kcal/mol reported for the concerted mechanism of retro-DA reactions [48,49]. Thus, the use of explicit external forces during QM/MM SMD simulations enables us to achieve an extended reactive intermediate that is beyond the scope of classical MD or non-equilibrium MD simulations, capturing thermally accessible retro-DA pathways even at a semi-empirical level of theory. We expect from extrapolation of forces (Fig. S8) that reducing the pulling speed will cause the barrier height and rupture forces to converge to even lower values, however, such simulations are currently limited by computing time.

To observe the effect of the PEG linker length on the dynamics and reaction mechanism, we also performed QM/MM SMD simulations for mechanophore with one and six PEG units. While a concerted mechanism is observed in both cases, the activation energy values and bond breaking forces are different (Fig. S9). For the mechanophore with one PEG unit, the end-to-end distance increases from 28.12 Å to 44.31 Å, beyond which the C1-C6 and the C4-C5 bonds break simultaneously. The reaction barrier is ~24.04 ± 2.54 kcal/mol, which is comparable to the values obtained from a three PEG linker in Fig. 3. For the mechanophore with six PEG units, the end-to-end distance increases from 35.99 Å to 62.83 Å, whereupon the molecule undergoes a retro-DA through a concerted mechanism. Here, the reaction barrier is ~32.10 ± 2.06 kcal/mol. Interestingly, the bond-breaking forces are 2.82 nN with one PEG unit and 3.84 nN with six PEG units when compared to the molecule with three PEG units, suggesting that varying the PEG length can be used to tune the force-sensing capability of the mechanophore.

To explore the relationship between mechanophore elongation and activation energy, we examined retro-DA reactions for unsubstituted mechanophores with 1, 3, or 6 PEG units using a pre-stretched linker geometries. We performed potential energy scan calculations at the B3LYP/6-31G//PM3 level of theory. While the activation energies for the retro-DA step are similar for all three PEG lengths (27.94, 28.62 and 28.24 kcal/mol, respectively) (Table S4), their values are ~4–9 kcal/mol lower than for the unstretched conformations (Table S2). When starting from an extended conformation, the all-atom RMSD values for all molecules (including their PEG units) are also similar for all three molecules. These observations suggest that linker elongation is a determining factor in the mechanophore reaction mechanism under external force.

2.4. Molecular dynamics models offer physically accurate estimates of mechanophore forces and energy changes

While QM/MM-SMD simulations offer realistic energy barriers, the high pulling speeds in these calculations can lead to an overestimation of the corresponding forces. Therefore, to obtain reliable force estimates for mechanophore activation, we benchmarked the force estimates from SMD against those from the constrained Geometries simulate External Force (CoGEF) method [50] (see Methods **M.3**). CoGEF has emerged as one of the most commonly used and straightforward methods to simulate the effect of mechanical force on structure of a molecule irrespective of the pulling rate [51]. It has been applied extensively for studying mechanochemical processes, such as retro-electrocyclization and retro-DA reactions. In the CoGEF method, the distance between two atoms experiencing a tensile force is increased in small steps and a relaxed geometry optimization is carried out at the QM level at each step. The slope of the energy of the system *vs* the distance between termini is calculated to determine the bond rupture force and to identify the atoms involved in bond breaking. Accordingly, by including CoGEF in our workflow, we can quantify the changes in critical force as a function of the substituents on the mechanophore and the length of the PEG linker.

We first performed CoGEF calculations for a previously established "minimal model" mechanophore [51] at the PM3 and B3LYP/6-31G levels of theory. As outlined in Figure S10, this model was constructed by substituting the fluorophore moiety with a methyl group, replacing the N substituent of the maleimide with an acetylated ethanol group, and capping the methanol substituent at C1 of the furan with an acetate group. For this model system, both levels of theory produced comparable values for the energy barrier to bond reorganization and retro-DA. In view of this benchmark, we went beyond the minimal model and used PM3 with CoGEF to simulate a complete unsubstituted mechanophore molecule with three PEG units. A recent study investigated the retro-DA reaction of a furan-maleimide adduct using CoGEF and found that the reaction proceeds via a diradical sequential process under external mechanical force [24]. The study was carried out at the UDFT/6-31G(d,p) level of theory. Interestingly, the model truncated

mechanophore (C44, Figure S10) also showed a sequential mechanism at this level of theory. We find that the absolute activation energy value is lower for the concerted than the sequential mechanism (Table S5). While both mechanisms may be possible, the concerted mechanism is kinetically more favoured, akin to Fig. 2.

The value of the bond rupturing force, F_{max}, determined from the slope of the energy *vs.* displacement curve of the complete mechanophore [51], was calculated to be approximately 3.13 nN, very much in the 2.8–3.8 nN range estimated by QM/MM-SMD (Fig. 4). The C1-C6 and C4-C5 bonds of the furan-maleimide adduct are the preferred reactive site upon mechanical elongation, which is consistent with the calculations of Fig. 3. Intermittent geometries from the calculations indicate that the furan-maleimide adduct undergoes a retro-DA reaction only when the molecule is mechanically stretched [51]. Notably, the end-to-end distance of the mechanophore increases from 34.82 Å in the equilibrium geometry to about 54.75 Å prior to maximum energy, consistent with what we observe in our equilibrium MD simulations (Fig. S11). After stretching, the mechanophore undergoes bond rupture, leading to the generation of the furfuryl carbonate.

A caveat of these CoGEF computations is that the E_{max} value for the mechanophore (237.51 kcal/mol) is much higher than the E_{max} calculated for the minimal model (62.63 kcal/mol) and our estimates from QM/MM SMD (23.57 kcal/mol). This finding is in line with a recent study of over 150 molecules, which found that while CoGEF calculations provide F_{max} values of high correlation with the experimental data, the associated E_{max} values are not reliable indicators of mechanochemical activity [51]. Furthermore, we did not find any systematic trend between the force estimation and CoGEF step size (Table S7), unlike in QM/MM SMD where the forces increase with pulling rate (Fig. S8). Thus, CoGEF offers refined force estimates at the cost of overestimating the barriers, whereas QM/MM-SMD provides both reliable values of mechanophore bond-rupture barriers as well as their forces under physically relevant solvation and temperature conditions.

2.5. *Mechanophore force sensing grows continuously with PEG linker length*

Our calculations indicate that the rate-determining step and the kinetics of the retro-DA can be modulated by either substituting the 3-position of the furan or varying the PEG unit length of the mechanophore. To further explore this observation, we computed the bond rupturing force for furan-maleimide mechanophores bearing various PEG linker lengths and a methyl or a phenoxy substituent at C3 of the furan unit using our semi-empirical CoGEF method (Figure S5D-S5E). With each C3 substituent, the PEG_3 mechanophore undergoes the retro-DA reaction. Interestingly, these calculations show that the bond-rupturing force F_{max} with the C3 methyl and phenoxy substituents does not vary significantly as compared to the unsubstituted furan, yielding values of 3.43 and 3.82 nN, respectively. Therefore, while the phenoxy substituent switches the rate-determining step from the fragmentation step to the mechanosensitive retro-DA reaction, it does not assist in force sensing of this reaction by tuning the F_{max} for breaking the C1-C6 or C4-C5 bonds.

Next, we explored the possibility of co-tuning the rate-determining step and the force-sensing step in mechanophore activation by changing the PEG linker length. We varied the number of PEG units from one to six repeats and used our semi-empirical CoGEF method to compute the bond-rupturing force F_{max} (see Methods **M.3**). Interestingly, F_{max} was found to increase almost quadratically with the PEG length (Fig. 5A). As expected, in this hybrid simulation scheme we find that mechanophores with higher linker lengths consistently react at larger end-to-end distances. The corresponding increase in F_{max} is attributed to the cost of the larger elongation or reorganization needed before the mechanophore undergoes the retro-DA reaction. As illustrated in Fig. 5B, as PEG repeats are added the E_{max} value increases with increasing end-to-end distance in the mechanophore conformation prior to bond breaking. This observation is also in line with the energy values from QM/MM SMD (Fig. S9). However, the local geometry prior to the bond-rupturing event and bond distances between the atoms undergoing the retro-DA reaction are comparable for all PEG lengths (Fig. 5C). Thus, achieving the extended reactive intermediate incurs a higher energy cost for longer PEG repeats, allowing the molecules of growing length to systematically sense stronger forces. Trends in both energy and forces are comparable with those from QM/

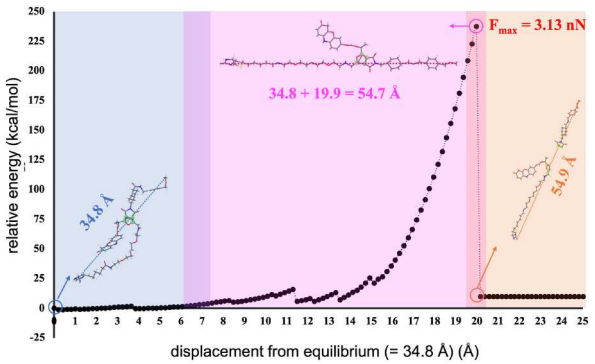

Fig. 4. Computation of the bond rupturing force in the retro-DA reaction. Energy profile of the mechanophore with respect to the distance from equilibrium geometry between terminal atoms O15 and C41, as obtained from the CoGEF calculations at the PM3 level of theory. Mechanophore conformations along the reaction coordinate (dashed lines) and atoms involved in bond-rupturing (green spheres) are highlighted. Conformational landscapes representing the reactant, transition state and product are highlighted with blue, magenta, and orange backgrounds, respectively.

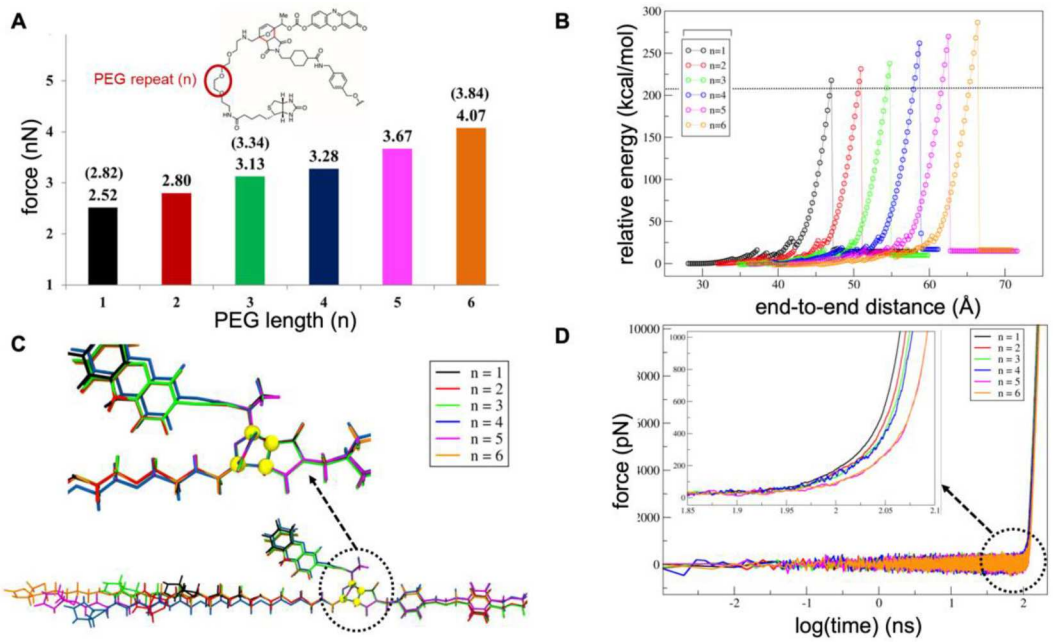

Fig. 5. Calibration of mechanochemical force. **A.** Bond-rupturing force for mechanophores with different PEG repeats obtained from CoGEF calculations at the PM3 level of theory. (corresponding values for one, three and six PEG as obtained from QM/MM SMD) **B.** Relative energy profiles for all six mechanophores with respect to distance between the terminal carbon atoms. **C.** Overlay of mechanophore geometries immediately prior to bond rupture in CoGEF calculations. The regions involved in the retro-DA reaction are highlighted. **D.** Force on Gly1 vs linker end-to-end distance, as calculated from classical SMD simulations of mechanophores with different numbers of PEG repeats. In these simulations, O15 of mechanophore was fixed and Gly1 was pulled at a constant velocity of 3 Å/ns. The region around the bond-breaking time is highlighted in the inset.

MM SMD (Fig. S9). However, the energy values are more refined in the latter with the reaction barrier for six PEG units is computed to be 37.60 kcal/mol in QM/MM SMD and 275.8 kcal/mol from CoGEF calculations.

2.6. Polypeptide-linked mechanophores are amenable to AFM calibration

To enable experimental calibration of the force required for mechanochemical fluorophore release, we sought to design a mechanophore compatible with single molecule atomic force microscopy (AFM) experiments. AFM is routinely employed to study the chemical and conformational changes of macromolecules under the influence of mechanical forces [52–54]. For these experiments, a spatial extension around 30 nm between the AFM tip and the mechanophore is chosen, noting that normally anywhere between 10 and 60 nm extension is experimentally required to distinguish specific mechanical properties [55]. While PEG is a popular, modular linker for cellular probes, multiple PEG units can decrease membrane permeability and hinder labeling of intracellular proteins. Therefore, we chose to exploit genetically encodable poly(GGGGS) linkers to tether the mechanophore to proteins of interest at relevant lengths. For this, we considered that the cellular forces inducing the reaction (typically 1 pN–100 nN) [56] and the force detection limit of AFM experiments (pN) [57] must be matched for successful imaging.

Our CoGEF calculations indicate that retro-DA reaction of a C3-unsubstituted, PEG_3-linked mechanophore requires an activation force of 3.13 nN. However, the impact of solvation, linker-length, pulling speed (step size) and temperature in reducing the barrier of the reaction within experimental conditions is not considered. So, the force estimates needed to bring forth the retro DA reaction derived from CoGEF will deviate from those of QM/MM SMD when the settings in SMD become more consistent with the experimental conditions. Hence, to overcome the limited applicability of CoGEF we used SMD simulations to determine the length of a poly(GGGGS) linker, and seek whether this would maintain the necessary sub-nanonewton rupture force on the mechanophore during constant velocity pulling while offering adequate time and length scales to execute AFM imaging measurements.

To achieve the 30 nm spatial extension for AFM measurements, we constructed initial models of the GGGGS linkers using the I-TASSER server (Fig. S12A). We found that a 20-mer repeat polymer was adequate to offer this linker length. To model a poly(GGGGS) linker in our mechanophore calculations, we introduced a covalent bond between C41 of the substituent on the maleimide and the side chain of the fifth serine residue of the 20th polymeric repeat (Ser100) (Fig. S12D). In a QM/MM-SMD simulation of the complete linker-mechanophore system, we pulled Gly1 of the poly(GGGGS) linker with a constant velocity while keeping the terminal O15 atom of biotin tether fixed (Fig. S13A). The QM region (157 atoms), comprised of our C3-unsubstituted mechanophore and a PEG_3 linker, was described at the semi-empirical PM3 level of theory. The MM region (213129 atoms), consisting of the poly(GGGGS) linker residues and surrounding water molecules, was described using the CHARMM36m force field. A pulling velocity of 2 Å/ps was employed to accommodate the large system size and MD integration steps, and the overall simulation was performed for 350 ps (Fig. 3,

Fig. S12F).

Our simulations show that the linker unfolds as the simulation progresses while the mechanophore remains stable until 225 ps. At this point, the linker has extended from 36.87 to 476.54 Å and the C1-C6 and C4-C5 bonds rupture simultaneously, indicating a retro-DA reaction. Notably, this corresponds to an O15 to C41 distance of ~53 Å in the mechanophore (Fig. S13B), which is similar to the stretched conformation seen in Fig. 3 in the absence of the poly(GGGGS) linker. Analysis of the electronic energy of the QM region shows a sharp increase from ~-35.92 ± 2.19 kcal/mol to ~ -4 kcal/mol at the bond-rupturing point (Fig. S13C). After unfolding, the Gly1 residue experiences a force of 6.6–7.8 nN, while the Ser100 and C41 atoms that are closer to the reaction center experience marginally weaker forces of 1.0–1.8 nN.

To refine these estimates further, we performed classical SMD of the linker-mechanophore system using a 1500-fold slower pulling speed of 3 Å/ns for 100 ns to arrive at an intermediate conformation with a mechanophore C15-O41 distance of 37.23 Å (Fig. 6). From this extended linker-mechanophore intermediate, we performed QM/MM-SMD simulations with a pulling speed of 60 Å/ns, identical to the pulling speed used for the PEG_3 mechanophore system in Fig. 3. At this pulling rate, the barrier to the retro-DA reaction decreases to ~23.88 ± 2.42 kcal/mol and the force estimates fall to 3.41 nN on Gly1, 0.9 nN on Ser100, and 0.87 nN on C41. The force estimate for this extended structure of mechanophore was computed to be 3.11 nN on C41 using CoGEF calculations with step-size of 0.2 Å.

As presented in Fig. S12F, a lower pulling speed enables more flexibility of the linker and enhanced sampling of the mechanophore conformations. Thus, for the classical SMD trajectory with a pulling speed of 3 Å/ns, the retro-DA reaction occurs at a poly(GGGGS) linker end-to-end distance of ~385 Å, which is ~90 Å shorter than the end-to-end distance using QM/MM-SMD at a speed of 60 Å/ns (Fig. S12F). These results show that the retro-DA reaction of the linker-mechanophore system is achieved with lower energy and force expenditures at lower pulling speeds (Fig. S15). Notably, when starting with a pre-extended poly(GGGGS) linker, both the energy and force values required to induce the retro-DA reaction are similar to those for the PEG_3-only mechanophore in Fig. 3.

Changes in retro-DA reaction barrier and activation forces with lower temperatures and smaller linker length are consistent with those of faster pulling speeds (Fig. S16, Table S6). Namely, at lower temperatures the linker becomes less dynamic, requiring a larger force to induce the reaction. Similarly, with a smaller linker length, linker dynamics contribute less towards activating the mechanophore, in turn leading to higher forces, with highest being for one seen in the mechanophore-only system at 3.18 nN (four-fold higher than the forces determined with our slowest SMD with the longest linker). So, models that capture alternate conformations to achieve the reaction barriers offer a more realistic estimate of the forces sensed by the mechanophore in biochemical environments.

In order to improve the accuracy of force estimation with the poly(GGGGS)-linked mechanophore system we reduced the pulling speed further, which required us to use a fully classical model. Thus, we performed SMD simulations with pulling speeds of 20 Å/ns and

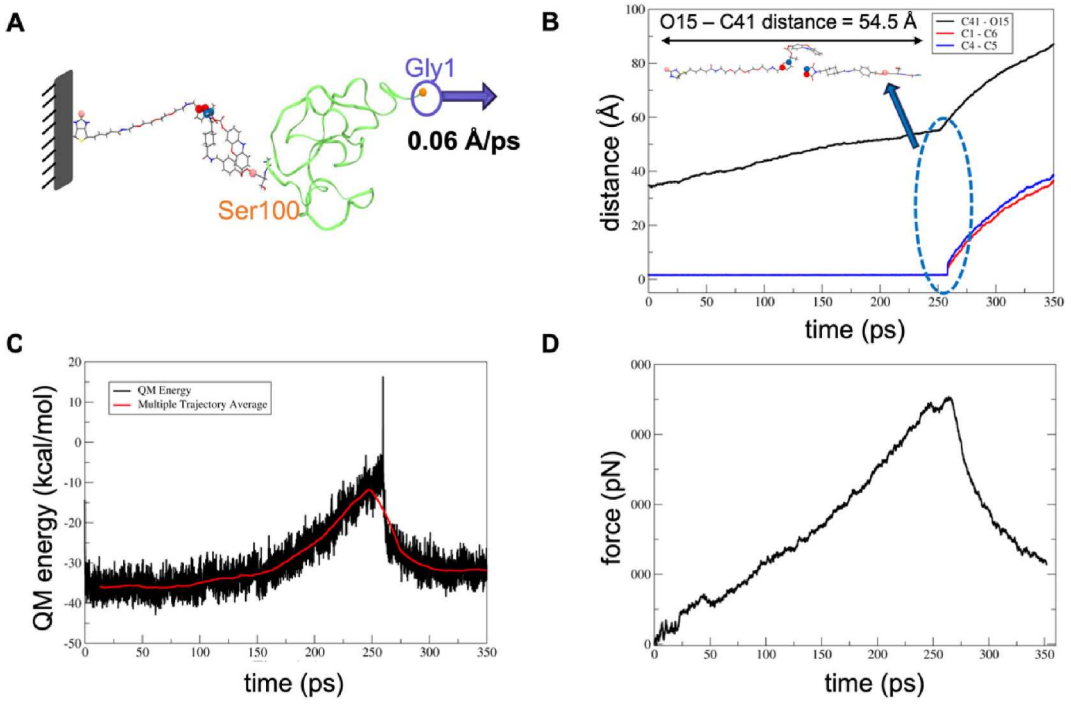

Fig. 6. Energy and force calculations for retro-DA of a poly(GGGGS)-linked mechanophore. **A.** Image of the initial state of the system used for QM/MM/SMD simulations of the mechanophore-linker complex. The mechanophore up to the terminal O15 atom was studied at the PM3 level of theory and the remaining atoms of the complex were considered at the MM level of theory. **B.** Plot of the end-to-end distance of the mechanophore (O15-C41) and bonds involved in the retro-DA reaction (C1-C6/C4-C5) in QM/MM/SMD simulations. **C.** Electronic energy of the QM region over time. **D.** Force on the atom Gly1 over time during the QM/MM SMD simulation.

3 Å/ns, and also at 300 Å/ns as a control. In these simulations, the force experienced by Gly1 beyond the unfolding stage is in the 0.2–0.5 nN range (Fig. S12C). Similarly, the Ser100 linker endures a force of 0.42 nN and C41 experiences a force of 0.36 nN. Comparison of F_{max} for these simulations shows that a lower pulling speed results in larger end-to-end distance intervals over which a sub-1 nN force distribution is achieved, which is sufficient for the inducing reaction cascade in mechanophore (Fig. S14). For instance, at a 3 Å/ns pulling speed, a sub-nN forces can be achieved over 95 ns, whereas at a speed of 300 Å/ns the force rapidly increased to nearly 2 nN over the first 1 ns (Fig. S14). This force saturates between 0.2 and 0.1 nN when our results are extrapolated to lower speeds between 0.1-0.01 Å/ns (Fig. S17A). These speeds are now achievable using high-speed AFM. However, since experimentally viable pulling are even slower ($10^{-4} - 10^{-7}$ Å/ns) [2] (Fig. S17B) [58–60], our results suggest that the mechanophore system requires a linker of length >30 nm to allow calibrated imaging of mechanical processes occurring on the millisecond to seconds timescale.

3. Conclusions

In this study we introduced a multiscale modeling approach to study mechanochemical probes in systems for cellular force sensing. Specifically, this approach enables the analysis of bio-compatible mechanophore systems in realistic environments, which considers the role of external force together with explicit solvent, variations in tether flexibility and temperature variations. We introduce a general force sensor design that can use a chemical genetic fusion tag (e.g., a HALO tag) to tether one end of a small molecule mechanophore to a protein of interest (e.g., and integrin or a mechanosensitive channel) and a biotin anchor to tether the other end of a biological substrate (e.g., the extracellular matrix or the nuclear envelope). The force-sensing unit of the mechanophore comprises a furan-maleimide adduct bound to a caged fluorophore, which undergoes a mechanically-induced retro-DA reaction to trigger fluorophore uncaging. To offer a multi-dimensional model of these mechanophores in a biological context, we devised a computational scheme that combines the strengths of three distinct methods. First, we employ high-level DFT and QM methods with MD-equilibrated geometries of mechanophore molecules to determine reaction mechanism starting from a local energy minimum in structure space. Second, we introduce CoGEF computations of the reactive geometries to benchmark QM/MM-SMD estimated forces required to induce mechanochemical bond-rupturing in simple systems. Finally, using these multiscale SMD simulations, we reproduce these reaction pathways in explicit environments and in the presence of external forces to refine energy estimates. By repeating the three steps across a range of molecular architectures, we find that mechanophore substituents and linkers can be used to systematically control both the rate-determining step and activation threshold of the mechanochemical cascade. Though explicit membranes and proteins have not been employed in the current simulations, building upon past successes of all atom SMD simulations in capturing mechanotransduction interfaces [61–64], the QM/MM-SMD approach is generalizable to much larger system sizes that include the chemical genetic fusion tag, protein of interest, and biological substrate in the MM region and the reactive mechanophore in the QM region.

We chose our combination of computational strategies to capitalize on the strengths and overcome the deficiencies of existing methods to study mechanochemical reaction mechanism, activation energies, and force thresholds. Specifically, while the QM/MM-SMD simulations enable modeling of large systems in realistic environments to offer continuous energy profiles with reasonable energy barriers, rupture force estimates can differ by orders of magnitude from comparable experimental systems. This discrepancy can be addressed by slower pulling velocities during SMD to match the computational and experimental set-ups, implying significant increase in simulation cost. Nonetheless, we show that sub-nN forces akin to the cellular environment [65,66] can still be accomplished with QM/MM-SMD of the mechanophores, albeit with semi-empirical approaches. Employing more sophisticated extensive sampling methods, such as metadynamics of adaptive biasing forces with the QM/MM interface is also feasible under the current framework, particularly within our NAMD engine [67]. By contrast, we find that CoGEF provides reasonable force estimates at fairly high levels of theory, but for simpler systems and consistently overestimates energy barriers by 2 to 3-fold relative to similar empirical systems. Thus, our approach makes it feasible to benchmark a SMD protocol that matches CoGEF for simple systems, and further extend the SMD protocols to determine geometries, energies, and forces that are commensurate with cellular processes and AFM measurements. Our probes offer a new paradigm for general, calibrated cellular force sensing with capabilities for quantitative tuning and multiplexing through chemical design. The computations reveal that the mechanophore itself can be activated with forces in the biologically relevant piconewton regime, however the unwinding of the tethers requires larger forces. So, we anticipate that these sensors will significantly expand our view of mechanical regulation in biological function, offering novel platforms to understand and control living systems.

CRediT authorship contribution statement

Sumit Mittal: Writing – original draft, Methodology, Investigation, Conceptualization. **Rongsheng E. Wang:** Writing – review & editing, Writing – original draft, Conceptualization. **Robert Ros:** Writing – review & editing, Conceptualization. **Alison E. Ondrus:** Writing – review & editing, Writing – original draft, Formal analysis, Conceptualization. **Abhishek Singharoy:** Writing – review & editing, Writing – original draft, Supervision, Methodology, Funding acquisition, Formal analysis, Data curation, Conceptualization.

Declaration of competing interest

The authors declare that they have no known competing financial interests or personal relationships that could have appeared to influence the work reported in this paper.

Acknowledgment

S.M. thanks the Science and Engineering Research Board (SERB, Department of Science and Technology, Government of India, New Delhi, India for financial support of the work (File no.: CRG/2022/002761). Funding support by the National Science Foundation (CHE-2144075) for R.E.W. is greatly appreciated. A.S. was supported by a CAREER award from the NSF (MCB-1942763) and an RO1 grant from the NIH (GM095583). A.S. also acknowledges funds from ASU-Mayo Foundation, AstraZenaca, and start-up grants from Arizona State University School of Molecular Sciences and Biodesign Institute's Center for Applied Structural Discovery. S.M. and A.S. thank the ASU Research Computing and their Agave computing cluster for computational resources. A.O, R.W and A.S jointly acknowledge Gordon and Betty Moore Foundation via a Scialo (#9162.07).

Appendix A. Supplementary data

Supplementary data to this article can be found online at https://doi.org/10.1016/j.heliyon.2024.e41178.

References

[1] A. Goujon, A. Colom, K. Straková, V. Mercier, D. Mahecic, S. Manley, N. Sakai, A. Roux, S. Matile, Mechanosensitive fluorescent probes to image membrane tension in mitochondria, endoplasmic reticulum, and lysosomes, J. Am. Chem. Soc. 141 (2019) 3380–3384, https://doi.org/10.1021/jacs.8b13189.
[2] Y. Liu, K. Galior, V.P.-Y. Ma, K. Salaita, Molecular tension probes for imaging forces at the cell surface, Acc. Chem. Res. 50 (2017) 2915–2924, https://doi.org/10.1021/acs.accounts.7b00305.
[3] C. Uhler, G.V. Shivashankar, Regulation of genome organization and gene expression by nuclear mechanotransduction, Nat. Rev. Mol. Cell Biol. 18 (2017) 717–727, https://doi.org/10.1038/nrm.2017.101.
[4] B. Liu, E.M. Kolawole, B.D. Evavold, Mechanobiology of T Cell activation: to catch a bond, Annu. Rev. Cell Dev. Biol. 37 (2021) 65–87, https://doi.org/10.1146/annurev-cellbio-120219-055100.
[5] D.H. Goldman, C.M. Kaiser, A. Milin, M. Righini, I. Tinoco, C. Bustamante, Mechanical force releases nascent chain–mediated ribosome arrest in vitro and in vivo, Science 348 (1979) 457–460, https://doi.org/10.1126/science.1261909, 2015.
[6] S.G. Alam, D. Lovett, D.I. Kim, K.J. Roux, R.B. Dickinson, T.P. Lele, The nucleus is an intracellular propagator of tensile forces in NIH 3T3 fibroblasts, J. Cell Sci. 128 (2015) 1901–1911, https://doi.org/10.1242/jcs.161703.
[7] K. Suffoletto, N. Ye, F. Meng, D. Verma, S.Z. Hua, Intracellular forces during guided cell growth on micropatterns using FRET measurement, J. Biomech. 48 (2015) 627–635, https://doi.org/10.1016/j.jbiomech.2014.12.051.
[8] S.A. Rashid, A.T. Blanchard, J.D. Combs, N. Fernandez, Y. Dong, H.C. Cho, K. Salaita, DNA tension probes show that cardiomyocyte maturation is sensitive to the piconewton traction forces transmitted by integrins, ACS Nano 16 (2022) 5335–5348, https://doi.org/10.1021/acsnano.1c04303.
[9] J. García-Calvo, J. López-Andarias, J. Maillard, V. Mercier, C. Roffay, A. Roux, A. Fürstenberg, N. Sakai, S. Matile, HydroFlipper membrane tension probes: imaging membrane hydration and mechanical compression simultaneously in living cells, Chem. Sci. 13 (2022) 2086–2093, https://doi.org/10.1039/D1SC05208J.
[10] P. Keshri, B. Zhao, T. Xie, Y. Bagheri, J. Chambers, Y. Sun, M. You, Quantitative and multiplexed fluorescence lifetime imaging of intercellular tensile forces, Angew. Chem. Int. Ed. 60 (2021) 15548–15555, https://doi.org/10.1002/anie.202103986.
[11] B. Zhao, N. Li, T. Xie, Y. Bagheri, C. Liang, P. Keshri, Y. Sun, M. You, Quantifying tensile forces at cell–cell junctions with a DNA-based fluorescent probe, Chem. Sci. 11 (2020) 8558–8566, https://doi.org/10.1039/D0SC01455A.
[12] L.S. Fischer, S. Rangarajan, T. Sadhanasatish, C. Grashoff, Molecular force measurement with tension sensors, Annu. Rev. Biophys. 50 (2021) 595–616, https://doi.org/10.1146/annurev-biophys-101920-064756.
[13] P. Roca-Cusachs, V. Conte, X. Trepat, Quantifying forces in cell biology, Nat. Cell Biol. 19 (2017) 742–751, https://doi.org/10.1038/ncb3564.
[14] A.-L. Cost, P. Ringer, A. Chrostek-Grashoff, C. Grashoff, How to measure molecular forces in cells: a guide to evaluating genetically-encoded FRET-based tension sensors, Cell. Mol. Bioeng. 8 (2015) 96–105, https://doi.org/10.1007/s12195-014-0368-1.
[15] R. Stevenson, G. De Bo, Controlling reactivity by geometry in retro-diels–alder reactions under tension, J. Am. Chem. Soc. 139 (2017) 16768–16771, https://doi.org/10.1021/jacs.7b08895.
[16] R. Nixon, G. De Bo, Three concomitant C–C dissociation pathways during the mechanical activation of an N-heterocyclic carbene precursor, Nat. Chem. 12 (2020) 826–831, https://doi.org/10.1038/s41557-020-0509-1.
[17] M.K. Beyer, H. Clausen-Schaumann, Mechanochemistry: the mechanical activation of covalent bonds, Chem Rev 105 (2005) 2921–2948, https://doi.org/10.1021/cr030697h.
[18] M. Stratigaki, R. Göstl, Methods for exerting and sensing force in polymer materials using mechanophores, Chempluschem 85 (2020) 1095–1103, https://doi.org/10.1002/cplu.201900737.
[19] P. Michael, W.H. Binder, A mechanochemically triggered "click" catalyst, Angew. Chem. Int. Ed. 54 (2015) 13918–13922, https://doi.org/10.1002/anie.201505678.
[20] J. Yang, M. Horst, J.A.H. Romaniuk, Z. Jin, L. Cegelski, Y. Xia, Benzoladderene mechanophores: synthesis, polymerization, and mechanochemical transformation, J. Am. Chem. Soc. 141 (2019) 6479–6483, https://doi.org/10.1021/jacs.9b01736.
[21] Z. Shi, J. Wu, Q. Song, R. Göstl, A. Herrmann, Toward drug release using polymer mechanochemical disulfide scission, J. Am. Chem. Soc. 142 (2020) 14725–14732, https://doi.org/10.1021/jacs.0c07077.
[22] R. Göstl, R.P. Sijbesma, π-extended anthracenes as sensitive probes for mechanical stress, Chem. Sci. 7 (2016) 370–375, https://doi.org/10.1039/C5SC03297K.
[23] X. Hu, T. Zeng, C.C. Husic, M.J. Robb, Mechanically triggered small molecule release from a masked furfuryl carbonate, J. Am. Chem. Soc. 141 (2019) 15018–15023, https://doi.org/10.1021/jacs.9b08663.
[24] M. Cardosa-Gutierrez, G. De Bo, A.-S. Duwez, F. Remacle, Bond breaking of furan–maleimide adducts via a diradical sequential mechanism under an external mechanical force, Chem. Sci. 14 (2023) 1263–1271, https://doi.org/10.1039/D2SC05051J.
[25] A. Semmeq, A. Monari, M. Badawi, S. Ouaskit, Ab initio study of the stepwise versus concerted fragmentation pathways in microhydrated thymine radical cations, Chem. Eur J. 25 (2019) 15525–15534, https://doi.org/10.1002/chem.201902462.
[26] S. Gupta, MdI. Alam, T.S. Khan, N. Sinha, M.A. Haider, On the mechanism of retro-Diels–Alder reaction of partially saturated 2-pyrones to produce biorenewable chemicals, RSC Adv. 6 (2016) 60433–60445, https://doi.org/10.1039/C6RA11697C.
[27] B. Ramirez, T. Cordova, F. Ruette, G. Chuchani, Inquiry of the reaction paths in thermal retro-Diels–Alder reactions in the gas phase: theoretical study on the concerted and stepwise elimination mechanisms of cyclohexenes, Comput Theor Chem 1067 (2015) 103–113, https://doi.org/10.1016/j.comptc.2015.05.017.
[28] L.L. Thomas, J. Tirado-Rives, W.L. Jorgensen, Quantum mechanical/molecular mechanical modeling finds Diels−Alder reactions are accelerated less on the surface of water than in water, J. Am. Chem. Soc. 132 (2010) 3097–3104, https://doi.org/10.1021/ja909740y.

[29] X. Hu, T. Zeng, C.C. Husic, M.J. Robb, Mechanically triggered release of functionally diverse molecular payloads from masked 2-furylcarbinol derivatives, ACS Cent. Sci. 7 (2021) 1216–1224, https://doi.org/10.1021/acscentsci.1c00460.

[30] T. Zeng, X. Hu, M.J. Robb, 5-Aryloxy substitution enables efficient mechanically triggered release from a synthetically accessible masked 2-furylcarbinol mechanophore, Chem. Commun. 57 (2021) 11173–11176, https://doi.org/10.1039/D1CC04886D.

[31] P. Dopieralski, P. Anjukandi, M. Rückert, M. Shiga, J. Ribas–Arino, D. Marx, On the role of polymer chains in transducing external mechanical forces to benzocyclobutene mechanophores, J. Mater. Chem. 21 (2011) 8309, https://doi.org/10.1039/c0jm03698f.

[32] J. Ribas-Arino, M. Shiga, D. Marx, Mechanochemical transduction of externally applied forces to mechanophores, J. Am. Chem. Soc. 132 (2010) 10609–10614, https://doi.org/10.1021/ja104958e.

[33] R. Car, M. Parrinello, Unified approach for molecular dynamics and density-functional theory, Phys. Rev. Lett. 55 (1985) 2471–2474, https://doi.org/10.1103/PhysRevLett.55.2471.

[34] J. Ribas-Arino, D. Marx, Covalent mechanochemistry: theoretical concepts and computational tools with applications to molecular nanomechanics, Chem Rev 112 (2012) 5412–5487, https://doi.org/10.1021/cr200399q.

[35] M.F. Iozzi, T. Helgaker, E. Uggerud, Influence of external force on properties and reactivity of disulfide bonds, J. Phys. Chem. A 115 (2011) 2308–2315, https://doi.org/10.1021/jp109428g.

[36] P. Dopieralski, J. Ribas-Arino, P. Anjukandi, M. Krupicka, D. Marx, Force-induced reversal of β-eliminations: stressed disulfide bonds in alkaline solution, Angew. Chem. Int. Ed. 55 (2016) 1304–1308, https://doi.org/10.1002/anie.201508005.

[37] P. Dopieralski, J. Ribas–Arino, P. Anjukandi, M. Krupicka, D. Marx, Unexpected mechanochemical complexity in the mechanistic scenarios of disulfide bond reduction in alkaline solution, Nat. Chem. 9 (2017) 164–170, https://doi.org/10.1038/nchem.2632.

[38] A.M. Saitta, P.D. Soper, E. Wasserman, M.L. Klein, Influence of a knot on the strength of a polymer strand, Nature 399 (1999) 46–48, https://doi.org/10.1038/19935.

[39] D. Aktah, I. Frank, Breaking bonds by mechanical stress: when do electrons decide for the other side? J. Am. Chem. Soc. 124 (2002) 3402–3406, https://doi.org/10.1021/ja004010b.

[40] T. Stauch, A. Dreuw, Advances in quantum mechanochemistry: electronic structure methods and force analysis, Chem Rev 116 (2016) 14137–14180, https://doi.org/10.1021/acs.chemrev.6b00458.

[41] G. Stirnemann, Recent advances and emerging challenges in the molecular modeling of mechanobiological processes, J. Phys. Chem. B 126 (2022) 1365–1374, https://doi.org/10.1021/acs.jpcb.1c10715.

[42] D. Gomez, W.J. Peña Ccoa, Y. Singh, E. Rojas, G.M. Hocky, Molecular paradigms for biological mechanosensing, J. Phys. Chem. B 125 (2021) 12115–12124, https://doi.org/10.1021/acs.jpcb.1c06330.

[43] M.C.R. Melo, R.C. Bernardi, T. Rudack, M. Scheurer, C. Riplinger, J.C. Phillips, J.D.C. Maia, G.B. Rocha, J. V Ribeiro, J.E. Stone, F. Neese, K. Schulten, Z. Luthey-Schulten, NAMD goes quantum: an integrative suite for hybrid simulations, Nat. Methods 15 (2018) 351–354, https://doi.org/10.1038/nmeth.4638.

[44] J. Zurek, A.L. Bowman, W.A. Sokalski, A.J. Mulholland, MM and QM/MM modeling of threonyl-tRNA synthetase: model testing and simulations, Struct. Chem. 15 (2004) 405–414, https://doi.org/10.1023/B:STUC.0000037896.80027.2c.

[45] F.J. Luque, N. Reuter, A. Cartier, M.F. Ruiz-López, Calibration of the quantum/classical Hamiltonian in semiempirical QM/MM AM1 and PM3 methods, J. Phys. Chem. A 104 (2000) 10923–10931, https://doi.org/10.1021/jp001974g.

[46] T.H. Musslimani, H. Mettee, AM1 and PM3 semi-empirical study of the Diels–Alder reaction between N-, P-, O- and S-substituted aromatic heterocyclic five-membered rings with acrolein, J. Mol. Struct.: THEOCHEM 672 (2004) 35–43, https://doi.org/10.1016/j.theochem.2003.11.018.

[47] L. Pacureanu, M. Mracec, Z. Simon, Aromatic heterocycles XII. Semiempirical PM3 study of Diels-Alder cycloaddition reaction of substituted phosphabenzenes, Open Chem. 2 (2004) 34–51, https://doi.org/10.2478/BF02476183.

[48] A.L. Widstrom, B.J. Lear, Structural and solvent control over activation parameters for a pair of retro Diels-Alder reactions, Sci. Rep. 9 (2019) 18267, https://doi.org/10.1038/s41598-019-54156-4.

[49] J. Carneiro de Oliveira, M.-P. Laborie, V. Roucoules, Thermodynamic and kinetic study of diels–alder reaction between furfuryl alcohol and N-Hydroxymaleimides—an assessment for materials application, Molecules 25 (2020) 243, https://doi.org/10.3390/molecules25020243.

[50] M.K. Beyer, The mechanical strength of a covalent bond calculated by density functional theory, J. Chem. Phys. 112 (2000) 7307–7312, https://doi.org/10.1063/1.481330.

[51] I.M. Klein, C.C. Husic, D.P. Kovács, N.J. Choquette, M.J. Robb, Validation of the CoGEF method as a predictive tool for polymer mechanochemistry, J. Am. Chem. Soc. 142 (2020) 16364–16381, https://doi.org/10.1021/jacs.0c06868.

[52] M. Ludwig, M. Rief, L. Schmidt, H. Li, F. Oesterhelt, M. Gautel, H.E. Gaub, AFM, a tool for single-molecule experiments, Appl. Phys. Mater. Sci. Process 68 (1999) 173–176, https://doi.org/10.1007/s003390050873.

[53] T.E. Fisher, A.F. Oberhauser, M. Carrion-Vazquez, P.E. Marszalek, J.M. Fernandez, The study of protein mechanics with the atomic force microscope, Trends Biochem. Sci. 24 (1999) 379–384, https://doi.org/10.1016/S0968-0004(99)01453-X.

[54] A.R. Sulkanen, J. Sung, M.J. Robb, J.S. Moore, N.R. Sottos, G. Liu, Spatially selective and density-controlled activation of interfacial mechanophores, J. Am. Chem. Soc. 141 (2019) 4080–4085, https://doi.org/10.1021/jacs.8b10257.

[55] D. Ebeling, B. Eslami, S.D.J. Solares, Visualizing the subsurface of soft matter: simultaneous topographical imaging, depth modulation, and compositional mapping with triple frequency atomic force microscopy, ACS Nano 7 (2013) 10387–10396, https://doi.org/10.1021/nn404845q.

[56] M. Prabhune, F. Rehfeldt, C.F. Schmidt, Molecular force sensors to measure stress in cells, J. Phys. D Appl. Phys. 50 (2017) 233001, https://doi.org/10.1088/1361-6463/aa6e1e.

[57] E. Thormann, T. Pettersson, P.M. Claesson, How to measure forces with atomic force microscopy without significant influence from nonlinear optical lever sensitivity, Rev. Sci. Instrum. 80 (2009) 093701, https://doi.org/10.1063/1.3194048.

[58] F. Eghiaian, F. Rico, A. Colom, I. Casuso, S. Scheuring, High-speed atomic force microscopy: imaging and force spectroscopy, FEBS Lett. 588 (2014) 3631–3638, https://doi.org/10.1016/j.febslet.2014.06.028.

[59] J. Hsin, J. Strümpfer, E.H. Lee, K. Schulten, Molecular origin of the hierarchical elasticity of titin: simulation, experiment, and theory, Annu. Rev. Biophys. 40 (2011) 187–203, https://doi.org/10.1146/annurev-biophys-072110-125325.

[60] F. Rico, L. Gonzalez, I. Casuso, M. Puig-Vidal, S. Scheuring, High-speed force spectroscopy unfolds titin at the velocity of molecular dynamics simulations, Science 342 (1979) 741–743, https://doi.org/10.1126/science.1239764, 2013.

[61] H. Lu, K. Schulten, The key event in force-induced unfolding of titin's immunoglobulin domains, Biophys. J. 79 (2000) 51–65, https://doi.org/10.1016/S0006-3495(00)76273-4.

[62] V.P. Hytönen, V. Vogel, How force might activate talin's vinculin binding sites: SMD reveals a structural mechanism, PLoS Comput. Biol. 4 (2008) e24, https://doi.org/10.1371/journal.pcbi.0040024.

[63] H. Lu, K. Schulten, Steered molecular dynamics simulations of force-induced protein domain unfolding, Protein Struct. Funct. Genet. 35 (1999) 453–463, https://doi.org/10.1002/(SICI)1097-0134(19990601)35:4<453::AID-PROT9>3.0.CO;2-M.

[64] E.H. Lee, J. Hsin, M. Sotomayor, G. Comellas, K. Schulten, Discovery through the computational microscope, Structure 17 (2009) 1295–1306, https://doi.org/10.1016/j.str.2009.09.001.

[65] Y. Liu, L. Blanchfield, V.P.-Y. Ma, R. Andargachew, K. Galior, Z. Liu, B. Evavold, K. Salaita, DNA-based nanoparticle tension sensors reveal that T-cell receptors transmit defined pN forces to their antigens for enhanced fidelity, Proc. Natl. Acad. Sci. USA 113 (2016) 5610–5615, https://doi.org/10.1073/pnas.1600163113.

[66] T. Iskratsch, H. Wolfenson, M.P. Sheetz, Appreciating force and shape — the rise of mechanotransduction in cell biology, Nat. Rev. Mol. Cell Biol. 15 (2014) 825–833, https://doi.org/10.1038/nrm3903.

[67] J.C. Phillips, R. Braun, W. Wang, J. Gumbart, E. Tajkhorshid, E. Villa, C. Chipot, R.D. Skeel, L. Kale, K. Schulten, Scalable molecular dynamics with NAMD, J. Comput. Chem. 26 (2005) 1781–1802.